IFASD 2015
International Forum on Aeroelasticity and Structural Dynamics
June 28 — July 02, 2015 ▲ Saint Petersburg, Russia

Theoretical and experimental investigation of a structurally and aerodynamically nonlinear pitch and flap wing

Edouard Verstraelen, Johan Boutet, Chiara Grappasonni, Gaetan Kerschen, and Grigorios Dimitriadis

Aerospace and Mechanical Engineering Department

Quartier Polytech 1 Allée de la découverte 9, 4000, Liège, Belgium

Keywords: Nonlinear Aeroelasticity, Wind tunnel testing, Dynamic stall, Stall flutter, Leishman-Beddoes.

Abstract:

This paper presents and experimental and theoretical investigation of a novel nonlinear aeroelastic system. It consists of a wing with pitch and flap degrees of freedom, suspended from a leaf spring secured in a nonlinear clamp. Both the structural and the aerodynamic forces acting on the wing can be nonlinear, depending on the amplitude of oscillations. Wind tunnel experiments show that the system undergoes a supercritical Hopf bifurcation that leads to small amplitude limit cycle oscillations. At a particular airspeed, the pitch amplitude jumps to a much higher value and dynamic stall starts to occur.

Three mathematical models of the system are formulated, one based on linear aerodynamics and two based on the Leishman-Beddoes dynamic stall model. The objective of the modelling is to determine whether the jump in pitch oscillation amplitude is due to dynamic stall. The predictions for amplitude, frequency and mean angle of the limit cycle oscillations are compared to the experimental observations. All three models predict the small amplitude oscillations with satisfactory accuracy. The complete Leishman-Beddoes model predicts the occurrence of a jump in pitch amplitude but the magnitude of this jump is significantly overestimated. The other two models completely fail to model the jump. The failure of the Leishman-Beddoes model to predict the correct post-jump oscillation amplitude may be due to the values selected for the model parameters.

1 INTRODUCTION

Aeroelasticity is the result of mutual interactions between the vibrating modes of a flexible structure and aerodynamic loads. It can lead to linear flutter or, in the nonlinear case, to limit cycle oscillations (LCOs) such as store-induced LCOs, transonic buzz and stall flutter. Such phenomena limit the performance or even the flight envelope of aircraft and have therefore been widely studied by the scientific community during the last 30 years.

Several authors have carried out experimental investigations of nonlinear aeroelastic phenomena. O'Neil et al.[1] built the Nonlinear Aeroelastic Testbed Apparatus (NATA), Conner et al.[2] investigated a typical aeroelastic section with pitch, plunge and control degrees of freedom (DOF) featuring freeplay, while Mukhopadhvay V.[3] developed the Pitch And Plunge Apparatus (PAPA) to investigate transonic aeroelasticity. More recent efforts include the works by Abdelkefi et al.[4] and Tang et al.[5]. Most of these investigations concentrated on structural nonlinear; aerodynamic nonlinearities such as stall flutter were investigated by several authors, including Dimitriadis and Li [6], Poirel et al.[7], Abdul Razak et al.[8] and Amandolese et al.[9].

Several of the experimental setups mentioned above use ball bearings, which also introduce nonlinear damping due to friction and hysteresis. The PAPA and the Poirel experiments avoid this problem by making use of flexible spring elements to suspend the wings. In this paper, a specially designed leaf spring and clamp assembly inspired by the work of Platten et al.[10] is used in order to provide nonlinear stiffness without bearings. The apparatus is referred to as the Nonlinear Pitch and Flap Wing (NLPFW). It is a flat plate with pitch and flap DOFs inspired by the Hancock wing [11]. Separation of the airflow occurs at high oscillation amplitudes, which also leads to aerodynamic nonlinearity.

This paper presents the NLPFW and provides an experimental and numerical investigation of its dynamic behaviour at both wind-off and wind-on conditions; particular emphasis is given to the appearance of stall flutter. Both linear and nonlinear aerodynamic models are used to predict the phenomena observed in the wind tunnel. The former is based on Wagner function aerodynamics while the latter is based on a modified version of the Leishman-Beddoes model [12] proposed by Sheng et. al. [13].

2 EXPERIMENTAL SETUP

The experimental apparatus is installed in the large low-speed wind tunnel of the University of Liège. It is designed to achieve very low damping ($\approx 0.3\%$ at wind-off conditions) and flutter at an airspeed of around 12m/s. To achieve such a low structural damping, the setup does not use any bearings or rotational springs. The pitch and flap restoring torques are provided by a specially designed leaf spring and nonlinear clamp assembly.
The complete NLPFW is shown in Fig. 1. It is a stiff thin rectangular unswept flat plate with span $s = 800$ mm, chord $c = 200$ mm, thickness $t = 4$ mm and an aspect ratio of 4. It is hinged at its root at $0.3c$ from the leading edge. As a result it features two rigid DOFs: a pitch rotation θ and a flap rotation γ, as shown in Fig. 2. The flexural axis, e_s, is parallel to the leading edge and passes by the hinge while the axis e_c is the root of the wing.

The stiffness in both pitch and flap is provided by a thin C75S leaf spring. It is 100 mm long, 70 mm large and 0.7 mm thick. It is clamped linearly to the flat plate and nonlinearly to the roof of the test section of the wind tunnel. Fig. 3(a) draws the geometry of the nonlinear roof clamps and Fig. 3(b) plots the nonlinear restoring torque of the pitch DOF. On the other hand, the flap stiffness is linear in the displacement range considered.

Finally, a 500 mm $\times$ 50 mm $\times$ 15 mm beam is bolted at the junction between the flat plate and the leaf spring (see Fig. 1(a) and 1(b)). It increases the rotational inertia of the system and consequently decreases its flutter speed to the target speed range: [10-15]

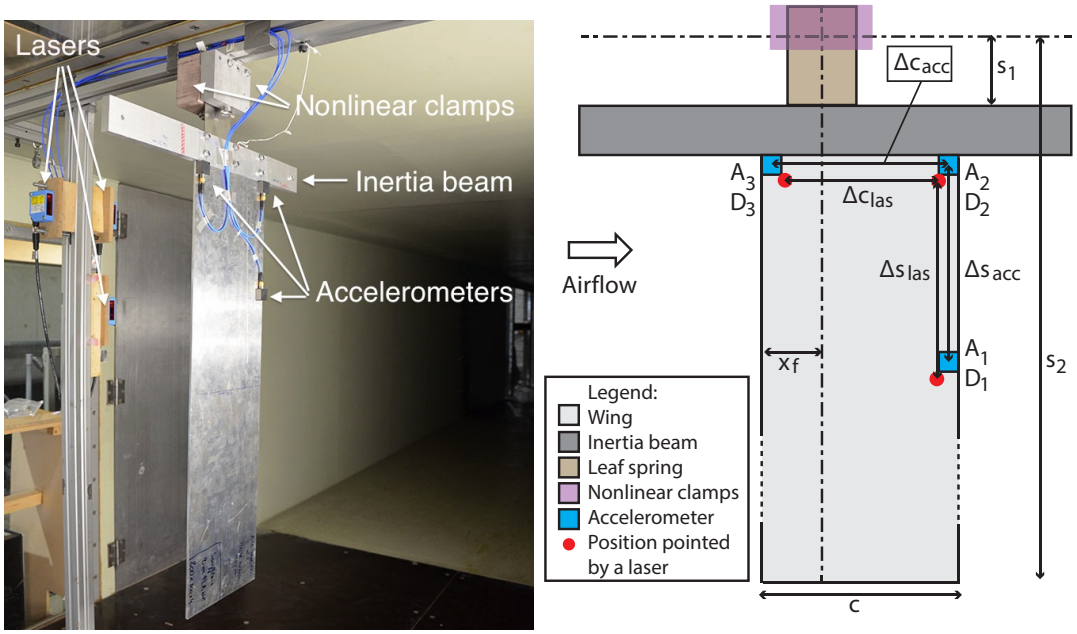

(a) Photo of the setup in the wind tunnel (b) Diagram showing transducer locations and major components of the NLPFW

Figure 1: Experimental setup showing wing, support and transducers

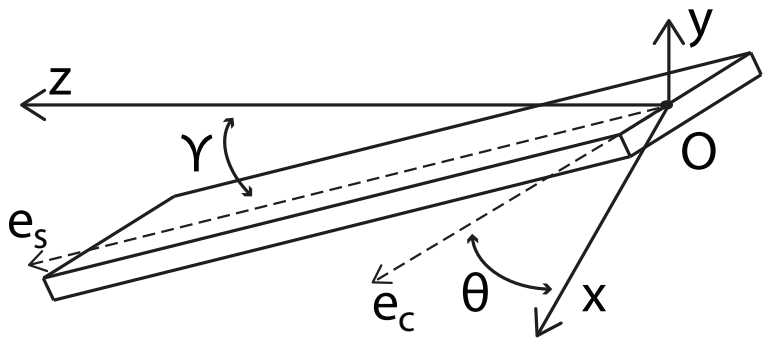

Figure 2: Schematic of the Hancock Wing

m/s. Table 1 summarises the wind-off characteristics of the NLPF.

The displacements are measured by the means of 3 Sick OD2-P300W200I0 laser sensors with a sensitivity of 9.6 mV/mm and a range of $100 - 500$ mm. The accelerations are measured using 3 MEMS DC accelerometers with a sensitivity of 100mV/g and a range of $\pm$ 30g. The sampling frequency of these two instruments is set to 1000Hz. The position of the sensors is shown in Fig. 1(b). The accelerometers A_2 & A_3 and the lasers D_2 & D_3 are placed at the root of the wing, where the torsion of the flat plate can be neglected.

3 EXPERIMENTAL RESULTS

3.1 Wind-off modal analysis of the system

A roving hammer test was carried out to identify the first few modes of the wind-off system. The wing was impacted five times in 24 different locations using a hammer

Caracteristic	Symbol	value	Unit
Dimensions of the wing:			
Span	s	800	[mm]
distance (flap axis - wing root)	s_1	65	[mm]
distance (flap axis - wing tip)	s_2	865	[mm]
Chord	c	200	[mm]
Half Chord	b	100	[mm]
Thickness	t	4	[mm]
Position of the center of mass	x_{cg}	$1/2c$	[mm]
Flap properties			
Linear stiffness	K_γ	≈ 5	[Nm/rad]
Inertia	I_γ	0.42	[kg m^2]
Damping	ζ_γ	≈ 1	[%]
Frequency	f_γ	0.85	[Hz]
Pitch properties			
Inertia	I_θ	0.029	[kg m^2]
Flexural axis position	x_f	$0.3c$	[mm]
Relative position of x_f and x_{cg}	a	$\frac{x_f - x_{cg}}{b}$	[-]
Linear stiffness coefficient	K_θ	10.1	[Nm/rad]
Quadratic stiffness coefficient	$K_{\theta,2}$	≈ 0	[Nm/rad^2]
Cubic stiffness coefficient	$K_{\theta,3}$	858	[Nm/rad^3]
Damping	ζ_θ	≈ 0.3	[%]
Frequency	f_θ	3.1	[Hz]
Position of the sensors			
Distance between A_1 and A_2	Δs_{acc}	200	[mm]
Distance between A_2 and A_3	Δc_{acc}	180	[mm]
Distance between D_1 and D_2	Δs_{las}	205.5	[mm]
Distance between D_2 and D_3	Δc_{acc}	168.5	[mm]

Table 1: Wind-off characteristics of the NLPF

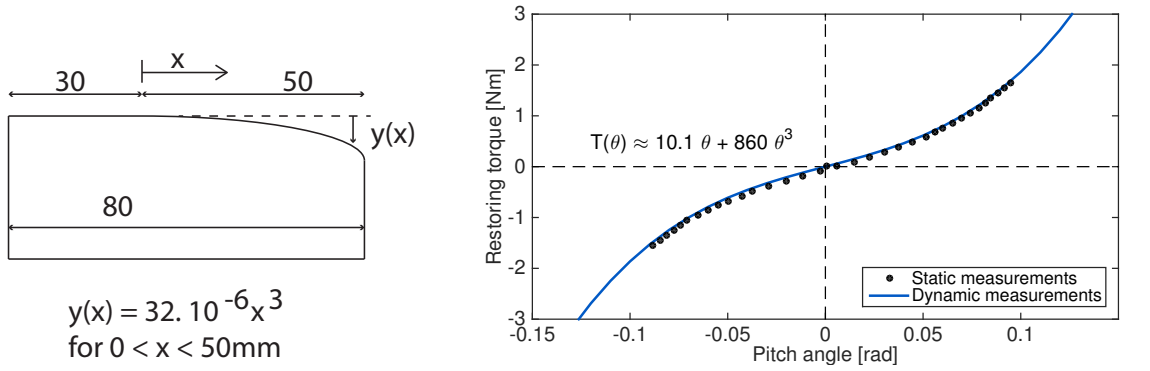

(a) Sketch of the clamps

(b) Experimental restoring torque curve of the pitch DOF

Figure 3: Characteristics of the nonlinear clamps

instrumented with a load cell. The response was measured with a single accelerometer placed on the trailing edge at the tip of the wing. Since it is very difficult to excite the leaf spring with the hammer its deflections are extracted from a model with shell finite elements of the whole structure computed by means of the Finite Element package SAMCEF. The first six modes are plotted in Fig. 4 and can be described as:

1. first flexural mode of the leaf spring and no deformation of the flat plate. It is equivalent to γ, the flap DOF of the Hancock wing.
2. first torsional mode of the leaf spring and no deformation of the flat plate. It is equivalent to θ, the pitch DOF of the Hancock Wing.
3. second flexural mode of the leaf spring and first flexural mode of the flat plate.
4. second flexural mode of the leaf spring and second flexural mode of the flat plate.
5. first torsional mode of the flat plate.
6. second flexural mode of the leaf spring and third flexural mode of the flat plate.

Shaker tests were also conducted but they did not provide any reliable results due to the absence of a suitable shaker support inside the wind tunnel. Moreover the NLPFW is designed to experience high displacements compared to the stroke of most electromagnetic shakers.

3.2 Wind-on study of the system

Fig. 5 displays the time response of the pitch rotation of the system at different airspeeds. Airspeeds of 0, 5.5 and 8.7 m/s lead to decaying response, as shown in Fig. 5(a). At airspeeds of 12.4, 13.3 and 14.8 m/s, Fig. 5(a) shows that the system undergoes Limit Cycle Oscillations.

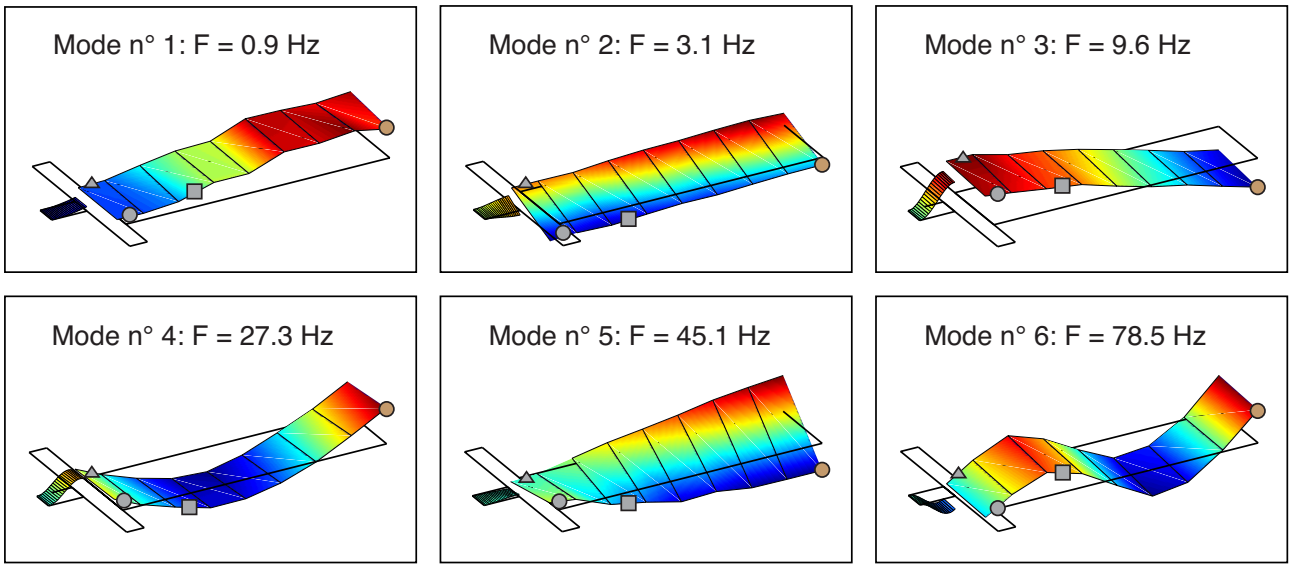

Figure 4: First six mode shapes of the NLPF.

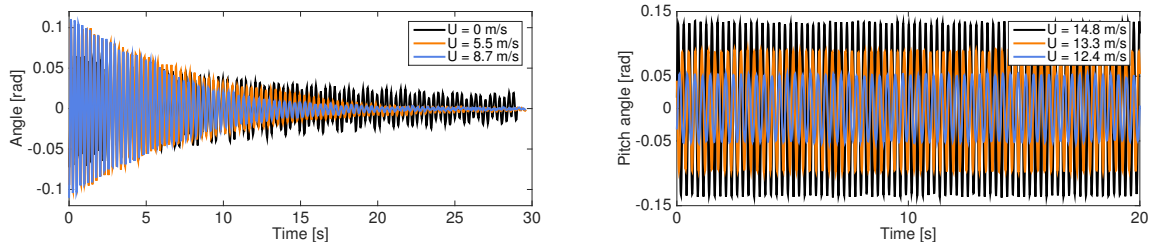

(a) Pitch subcritical response: free decay

(b) Pitch supercritical response: LCO

Figure 5: Time series of the pitch rotation at sub and super critical airspeeds

3.2.1 Variation of subcritical modal parameters with airspeed

At each stabilised subcritical airspeed, the system was given an initial pitch and flap angle then was released. Assuming a de-coupled linear decaying response, the time variation of the degrees of freedom can be written as a complex exponential whose imaginary part $\omega\sqrt{1-\zeta^2}$ is the damped frequency of the motion and whose real part $\zeta\omega$ is the effective damping:

$$\begin{aligned} \gamma(t) &= e^{\lambda_\gamma t} = e^{-\zeta_\gamma\omega_\gamma \pm i\omega_\gamma\sqrt{1-\zeta_\gamma^2}} \\ \theta(t) &= e^{\lambda_\theta t} = e^{-\zeta_\theta\omega_\theta \pm i\omega_\theta\sqrt{1-\zeta_\theta^2}} \end{aligned} \tag{1}$$

The imaginary part of λ was computed from these free decays using both Fast Fourier Transform (FFT) and Wavelet Analysis. The real part was extracted using an exponential curve fit of the Hilbert Transform of the responses. The variation of these real and imaginary parts with airspeed are typical of aeroelastic setups as displayed in Fig. 6: the pitch real part increases, is maximum at 9m/s then decreases until it reaches zero and flutter occurs. The flap real part increases strongly all the time. The flap frequency is approximately constant while the pitch frequency decreases until the modes can interact to cause flutter. The flap frequency resolution is very low and that the flap effective

damping measurements are very scattered because the aerodynamic damping was so high that the system could only undergo one or two oscillations before going back to rest.

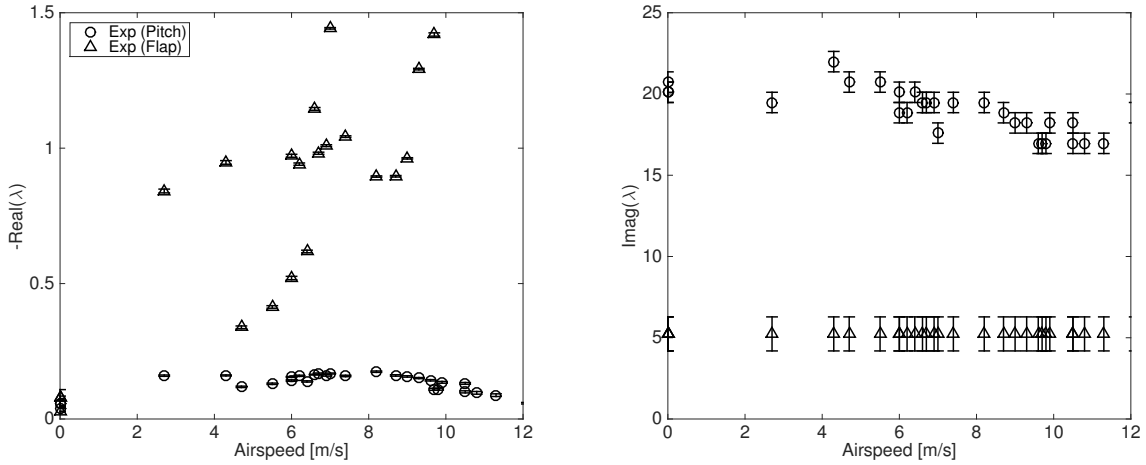

(a) Real part: effective damping

(b) Imaginary part: damped pulsation

Figure 6: Variation of the modal parameters of the pitch and flap DOFs with the airspeed before the flutter

3.2.2 Post-critical aeroelastic behaviour

The post-critical bifurcation diagram is displayed in Fig. 7, which plots limit cycle amplitude, frequency and mean angle in both pitch and flap. The black marks indicate increasing airspeed tests while they grey ones correspond to decreasing airspeed tests. There is no significant difference between the two sets of test points, which suggests that there is no hysteresis in the system.

Figs.7(a) & 7(c) respectively show the variation of pitch and flap LCO amplitude -defined as the half of the peak-to-peak amplitude- with airspeed, where the errorbars indicate the standard deviation around these averages. The bifurcation at 11.5 m/s is a supercritical Hopf: the LCOs were self-excited and manually exciting the system did not lead to a jump on a branch of higher amplitude. The flap amplitude increases smoothly with airspeed but the pitch amplitude features a jump around 13.5 m/s followed by a plateau. The pitch amplitude is roughly five times larger than that of the flap. This pitch domination of the motion was expected since section 3.2.1 highlighted that it is the pitch mode whose damping drops towards zero at flutter.

The variation of the LCO frequency with airspeed is displayed in Fig. 7(b). The frequency start at 2.5 Hz, increases steadily to approximately 3 Hz and then jumps to around 4.1 Hz and becomes stabilised. Finally the pitch and flap mean angles, depicted in Fig. 7(d), indicate the asymmetry of the LCOs. The pitch mean angle is negligible but that of the flap is not. Consequently, the flap oscillations are highly asymmetrical and the mean flap angle increases stadily with airspeed. This phenomenon is due to the asymmetry in the system: a small pitch displacement leads to a large flap moment which in turn causes a flap deflection that increases quadratically with airspeed.

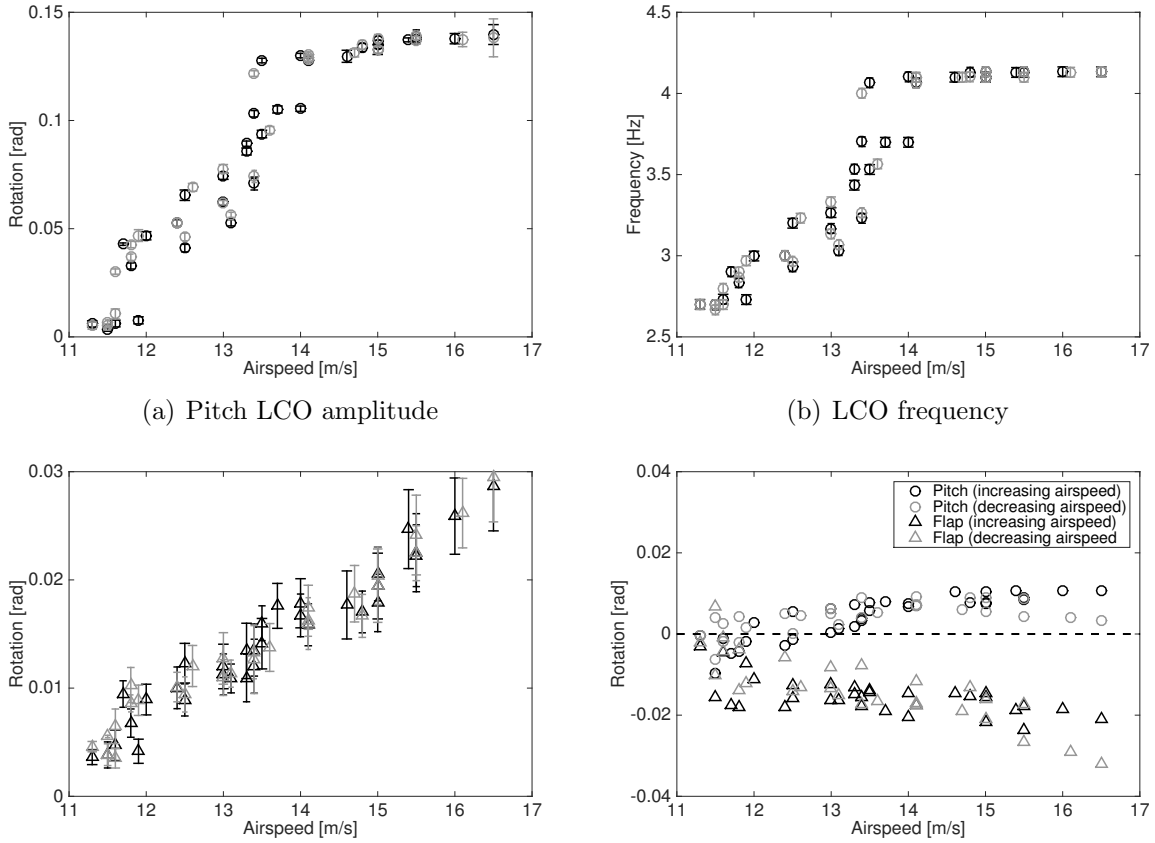

(a) Pitch LCO amplitude

(b) LCO frequency

(c) Flap LCO amplitude

(d) Pitch and Flap average angle

Figure 7: Bifurcation diagram of the system. The black marks indicate increase airspeeds and the grey ones show decreasing airspeeds

A test with wool tufts demonstated that separation of the airflow occurs after the jump to pitch amplitudes of around 8°. Figs. 8(b) to 8(e) show 4 pictures of the wool tufts placed as displayed in Fig. 8(a) at four time instances of the same half cycle. The top row of tufts, which corresponds to the red one in Fig. 8(a), lies near the leading edge of the wing while the bottom row, which corresponds to the green one, lies near the trailing edge. The following phenomena occur:

- t_1: the pitch angle is small and increasing, the tufts stick to the wing because the airflow is attached.
- t_2: the pitch angle is large and the front line of tufts (top) is detached from the wing which indicates separation of the airflow near the leading edge. The second line of tufts is much less affected by separation than the first line.
- t_3: the pitch angle is larger than at t_2. The airflow is now separated on both the leading and trailing edges.
- t_4: the pitch angle is small and the airflow is re-attached on the wing.

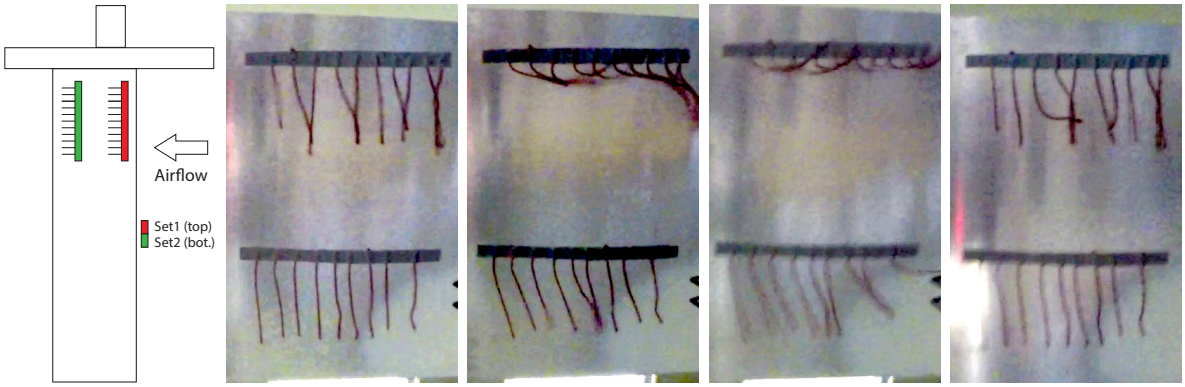

(a) Position of the tufts on the NLPF

(b) t_1: beginning of the half cycle, small increasing pitch angle and attached flow

(c) t_2: middle of the half cycle, large pitch angle & separation of the airflow on the leading edge

(d) t_3: middle of the half cycle, large pitch angle & separation of the airflow on both the leading and trailing edges

(e) t_4: end of the half cycle, small decreasing pitch angle and attached flow

Figure 8: Pictures of wool tufts on the wing during a cycle of half period of stall flutter at 14.9 m/s. The air flows from the top to the bottom on pictures (b) to (e).

3.2.3 Response frequency content variation with airspeed

The frequency content of the LCO responses at different airspeeds is represented in the waterfall plots of Fig. 9. Fig. 9(left) plots the pitch frequencies and features the following peaks:

- The fundamental frequency, f_0, lies at 2.9Hz at 11.5 m/s and reaches 4.1 Hz at 15.5 m/s. Its variation with airspeed was displayed in Fig. 7(b).
- A small third harmonic, $3f_0$, lies at 11.5m/s and its strength does not grow with airspeed compared to that of f_0.
- The fourth and sixth harmonics, $4f_0$ and $6f_0$ emerge after the jump (13.5 m/s) and their strengths do not grow with airspeed either.
- The fifth harmonic, $5f_0$ appears after the jump and its amplitude increases slightly with airspeed.

Fig. 9(right) displays the variation of the frequency content with airspeed, as measured from accelerometers A_1 & A_2. It features the following peaks:

- The fundamental frequency, f_0 lies at 2.9 Hz at 11.5 m/s and reaches 4.1 Hz at 15.5 m/s.
- The second harmonic, $2f_0$ contributes to the motion from 11.5m/s but its strength increases drastically after the jump.

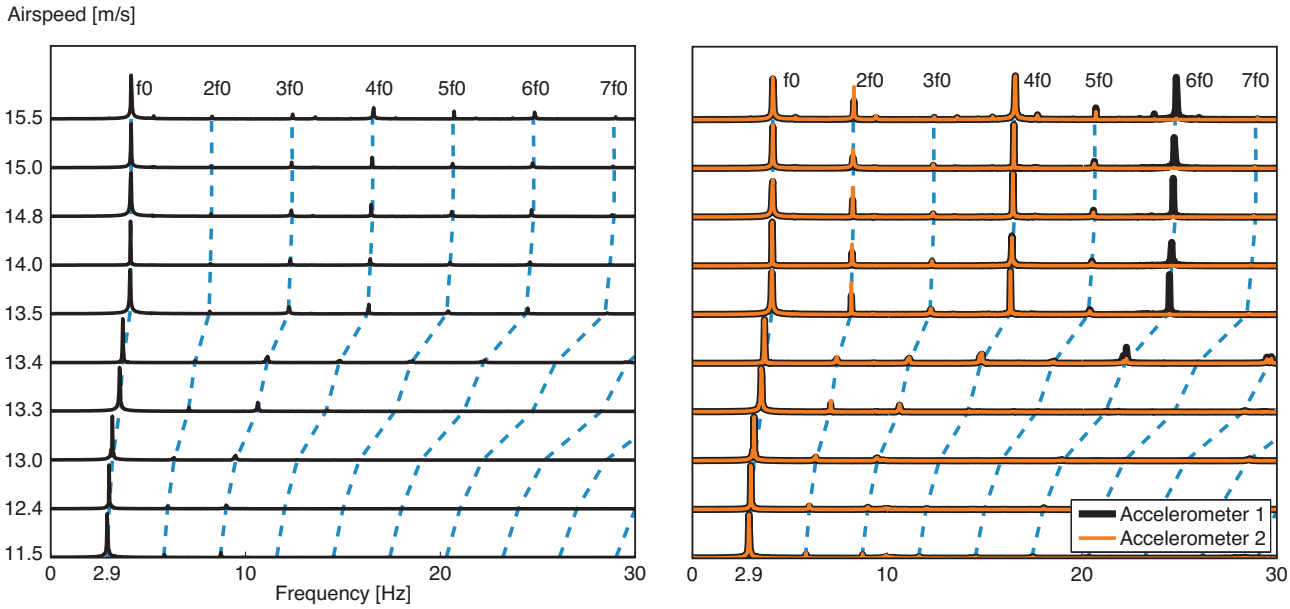

Figure 9: Waterfall plot of the pitch acceleration $\ddot{\theta}$ (left) and of the accelerations A_1 & A_2 (right)

- The fourth and sixth harmonics, $4f_0$ and $6f_0$ start at small amplitude right before the jump (13.4 m/s) and their strengths become similar to the strength of the fundamental harmonic after the jump (13.5 m/s). It is interesting to notice that the fourth harmonic is strong on both A_1 and A_2 while the sixth one is only measurable in A_1.
- The third and fifth harmonics and a few other small peaks emerge as the airspeed increases but their strength is very small and they to not contribute greatly to the dynamics of the system.

4 AEROELASTIC MODEL WITH LINEAR AERODYNAMICS

This section aims to model the low amplitude behaviour of the system: the subcritical response, investigated in section 3.2.1 and the low amplitude (before the jump) supercritical response investigated in section 3.2.2. It is carried out by means of a two-DOF model with a cubic hardening nonlinearity and linear aerodynamics obtained from strip theory and Wagner function aerodynamics.

The nonlinear pitch and flap wing is modeled as a two-DOF system, assuming that the flexible modes of the plate do not participate significantly in the observed aeroelastic phenomena. The structural nonlinear equations of motion are

$$\begin{pmatrix} I_\gamma & S \\ S & I_\theta \end{pmatrix} \begin{pmatrix} \ddot{\gamma} \\ \ddot{\theta} \end{pmatrix} + \begin{pmatrix} c_\gamma & c_{\gamma\theta} \\ c_{\gamma\theta} & c_\theta \end{pmatrix} \begin{pmatrix} \dot{\gamma} \\ \dot{\theta} \end{pmatrix} + \begin{pmatrix} k_\gamma & k_{\gamma\theta} \\ k_{\gamma\theta} & k_\theta \end{pmatrix} \begin{pmatrix} \gamma \\ \theta \end{pmatrix} + \begin{pmatrix} M_{\gamma,NL}(\gamma) \\ M_{\theta,NL}(\theta) \end{pmatrix} = \begin{pmatrix} M_{\gamma,\text{ext}}(t) \\ M_{\theta,\text{ext}}(t) \end{pmatrix} \quad (2)$$

$$\begin{aligned} M_{\gamma,NL} &= 0 \\ M_{\theta,NL} &= k_{nl,3}\theta^3 \end{aligned} \quad (3)$$

where the parameter values are given in table 1. A nonlinear torque is only applied to the pitch DOF and is a cubic function of pitch.

The flap and pitch aerodynamic moments are computed using strip theory (see for instance Bisplinghoff & al.[14]). It states that the total aerodynamic moments M_γ and M_θ acting on a finite wing are equal to the sum of the loads dL and dM acting on small spanwise strips of width dy. These infinitesimal forces and moments are computed assuming 2D aerodynamics. The strip theory assumption leads to the following formulation for the flap and pitch aerodynamic moments

$$M_\gamma = -\int_{s_1}^{s_2} y \; dL(t) \tag{4}$$

$$M_\theta = \int_{s_1}^{s_2} dM_\theta(t) \tag{5}$$

s_1 being the distance between the flap axis and the root of the wing and s_2 the distance between the flap axis and the tip of the wing. The lift force dL and pitch moment dM_θ of a strip can be computed using any unsteady aerodynamic formulation. Unsteady aerodynamics based on Wagner's function [15] was chosen here because the reduced frequency of oscillation $k = \frac{\omega b}{U} \approx 1.5 >> 0.02$ is too large to use quasi-steady aerodynamics and Theodorsen is defined in frequency domain which makes it difficult to use on a nonlinear system. The growth of circulation around a flat un-cambered airfoil after a step change of incidence is approximated by Wagner's function

$$\Phi(t) = 1 - \psi_1 e^{-\frac{\epsilon_1 U t}{b}} - \psi_2 e^{-\frac{\epsilon_2 U t}{b}} \tag{6}$$

Integrating equations 4 and 5 with Fung's lift and moment expressions [15] and applying Lee & al.[16]'s transformation to replace the wake integrals by aerodynamic state variables yields the complete equations of motion

$$\begin{bmatrix}
\begin{pmatrix} I_\gamma & S \\ S & I_\theta \end{pmatrix} + \rho\pi b^2 \begin{pmatrix} \Lambda^3/3 & -ab\Lambda^2/2 \\ -ab\Lambda^2/2 & b^2\Lambda(a^2+1/8) \end{pmatrix} \end{bmatrix} \begin{pmatrix} \ddot{\gamma} \\ \ddot{\theta} \end{pmatrix} + \\
\begin{bmatrix}
\begin{pmatrix} c_\gamma & c_{\gamma\theta} \\ c_{\gamma\theta} & c_\theta \end{pmatrix} + \rho\pi U b \begin{pmatrix} \frac{2}{3}\Phi(0)\Lambda^3 & b\Lambda^2[1/2 - \Phi(0)(1-a/2)] \\ -b\Lambda^2\Phi(0)(a+1/2) & -\Lambda b^2(a-1/2)[1+2\Phi(0)(a+1/2)] \end{pmatrix} \end{bmatrix} \begin{pmatrix} \dot{\gamma} \\ \dot{\theta} \end{pmatrix} + \\
\begin{bmatrix}
\begin{pmatrix} k_\gamma & k_{\gamma\theta} \\ k_{\gamma\theta} & k_\theta \end{pmatrix} + \rho\pi U^2 \begin{pmatrix} \frac{2}{3}\Lambda^3[\frac{b\dot{\Phi}(0)}{U}] & b\Lambda^2[\Phi(0) + \frac{b\dot{\Phi}(0)}{U}(1/2-a)] \\ -b\Lambda^2[\frac{b\dot{\Phi}(0)}{U}(a+1/2)] & -2\Lambda^3(a+1/2)[\Phi(0) - \frac{b\dot{\Phi}(0)}{U}(a-1/2)] \end{pmatrix} \end{bmatrix} \begin{pmatrix} \gamma \\ \theta \end{pmatrix} + \\
\begin{bmatrix}
\pi\rho U^3 \begin{pmatrix} -2\epsilon_1^2\psi_1\Lambda^3/3b & \epsilon_1^2\psi_1\Lambda^2(2a+1)/2 \\ -2\epsilon_2^2\psi_2\Lambda^3/3b & \epsilon_2^2\psi_2\Lambda^2(2a+1)/2 \\ \Lambda^2(\epsilon_1\psi_1 - \epsilon_1^2\psi_1/2 + a\epsilon_1^2\psi_1) & -2b\epsilon_1\psi_1\Lambda(a+1/2)(\epsilon_1(a-1/2)+1) \\ \Lambda^2(\epsilon_2\psi_2 - \epsilon_2^2\psi_2/2 + a\epsilon_2^2\psi_2) & -2b\epsilon_2\psi_2\Lambda(a+1/2)(\epsilon_2(a-1/2)+1) \end{pmatrix}^T \end{bmatrix} \begin{pmatrix} w_1 \\ w_2 \\ w_3 \\ w_4 \end{pmatrix} = \\
\begin{bmatrix}
\begin{pmatrix} M_{\gamma,ext}(t) \\ M_{\theta,ext}(t) \end{pmatrix} + 2\pi\rho U b\dot{\Phi}(t) \begin{pmatrix} \Lambda^3\gamma(0)/3 + (\frac{3b}{2} - x_f)\Lambda^2\theta(0)/2 \\ -(a+1/2)b[\Lambda^2\gamma(0)/2 + (\frac{3b}{2} - x_f)\Lambda\theta(0)] \end{pmatrix} - \begin{pmatrix} 0 \\ k_{nl,3}\theta^3 \end{pmatrix} \end{bmatrix}
\end{bmatrix} \tag{7}$$

with $\Lambda^j = s_2^j - s_1^j$. They feature structural and aerodynamic inertia, damping and stiffness matrices and an aerodynamic state matrix on the left hand side. The right hand side comprises three terms, one of which is the nonlinear pitch restoring torque. The external loads are set to zero because the system is self-excited. The second term is set to zero because it decays quickly in time and only the steady-state response is of interest. The nonlinear equations of motion are solved using a numerical continuation algorithm based on a finit difference formulation.

5 AEROELASTIC MODEL WITH MODIFIED LEISHMAN-BEDDOES MODEL

The model with linear aerodynamics from section 4 is unable to represent the amplitude jump observed experimentally. A nonlinear aerodynamic model was created in order to investigate if the jump is caused by dynamic stall. This alternate aerodynamic model is based on a modified version of the Leishman-Beddoes model [12] proposed by Sheng et. al. [13] (LB). The complete nonlinear aeroelastic system can be written as :

$$\begin{aligned} \mathbf{G}(\mathbf{u}\,,\mathbf{q}\,,\dot{\mathbf{q}},)\begin{bmatrix}\dot{\mathbf{u}}\\ \dot{\mathbf{q}}\\ \ddot{\mathbf{q}}\end{bmatrix} &= \mathbf{f}(\mathbf{u}\,,\mathbf{q}\,,\dot{\mathbf{q}}) \\ \mathbf{M}\ddot{\mathbf{q}}+\mathbf{C}\dot{\mathbf{q}}+\mathbf{K}\mathbf{q}+\begin{bmatrix}M_{\gamma,NL}(\gamma)\\ M_{\theta,NL}(\theta)\end{bmatrix} &= \mathcal{M}(\mathbf{u}\,,\mathbf{q}\,,\dot{\mathbf{q}}) \end{aligned} \tag{8}$$

where $\mathbf{u}$ are seven aerodynamic state variables for a given airfoil 2D section, $\mathbf{q}$ are the degrees of freedom in flap (γ) and pitch (θ) and the structural equations those given in equation 3.

5.1 Over view of the Leishman-Beddoes Model

The modified Leishman-Beddoes model can be split into three different modules as shown in figure 10. These modules are :

- **Attached flow module :** This module, based on Wagner unsteady aerodynamics, aims to compute the circulatory and impulsive normal loads acting on the airfoil. It will take as inputs:
  - The rigid airfoil section's flapping (γ) and pitching (θ) motion;
  - The airfoil's geometry.

  This module works under the assumption of unsteady incompressible conditions, which are defined by Leishman [17] as $Mk \ll 1$, where M is the Mach number and k is the reduced frequency.

- **Trailing edge separation module :** This module aims to compute the effect of trailing edge separation on the circulatory normal loads. It will take as inputs :
  - The airfoil's steady lift, drag and moment curves, in order to compute the functions $f(\alpha)$ and $g(f)$, representing the position of the separation point on the airfoil and the variation of the moment with separation point position, respectively;
  - A lag parameter (T_a);
  - The viscous lag parameter (T_f).

- **Vortex module :** This module aims to compute the normal load and moment induced by the vortex generated on the leading edge of the airfoil and the overshoot it can cause. It will take as inputs :
  - The vortex dissipation parameter (T_v);
  - The vortex shedding starting conditions;
  - The non-dimensional time taken by the vortex to travel over the airfoil (T_{vl}).

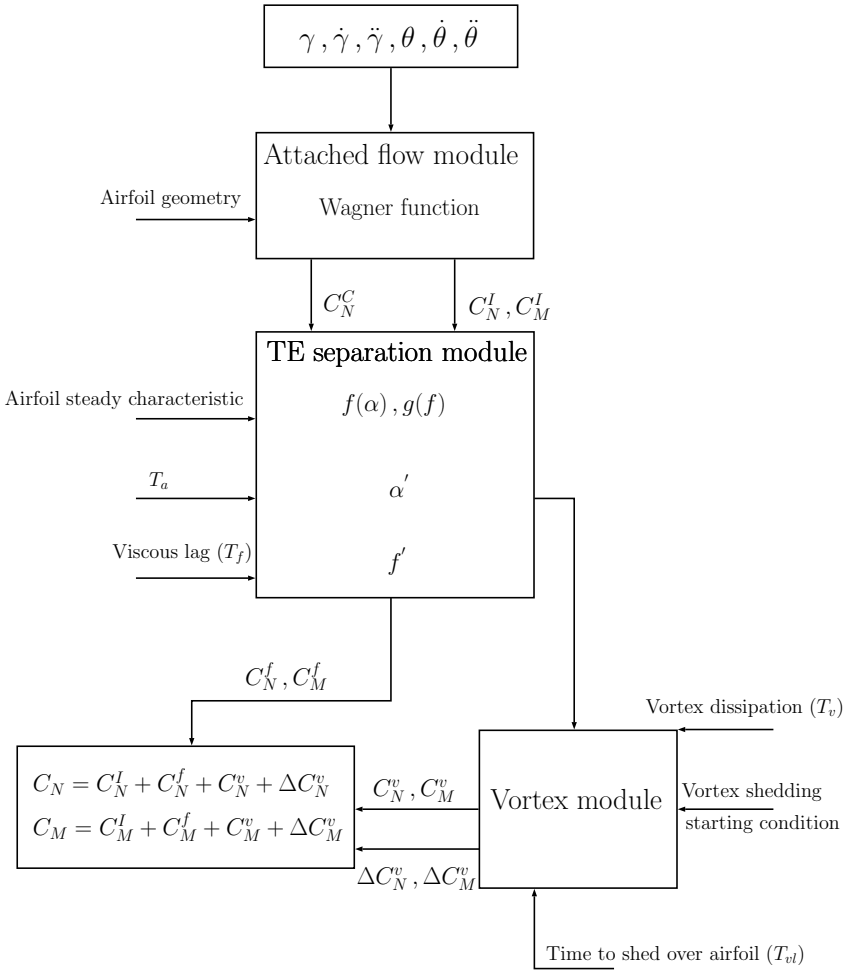

Figure 10: Leishman-Beddoes model flowchart

5.2 Modified trailing edge separation flow module

5.2.1 Computation of $f(\alpha)$

In order to compute the non linear behaviour of the lift generated by an airfoil, Leishman and Beddoes used the Kirchhoff-Helmholtz theory which approximates the normal lift coefficient by

$$C_n = C_{na}\,(\alpha - \alpha_0)\left(\frac{1+\sqrt{f(\alpha)}}{2}\right)^2 \quad \Leftrightarrow \quad f(\alpha) = \left(2\sqrt{\frac{C_n}{C_{na}(\alpha-\alpha_0)}} - 1\right)^2 \tag{9}$$

where C_{na} is the normal lift slope, α is the angle of attack, α_0 is the zero lift angle and f is the non-dimensional position of the separation point on the airfoil.

It is possible to compute discrete values of $f(\alpha)$ from steady aerodynamic data and equation 9. These discrete values can be curve-fitted by a chosen function. Leishman and Beddoes used a discontinuous exponential function, which lacks flexibility for asymmetrical airfoils. In the present work, cubic splines are used to fit $f(\alpha)$. Figure 11 plots the results of this curve-fit.

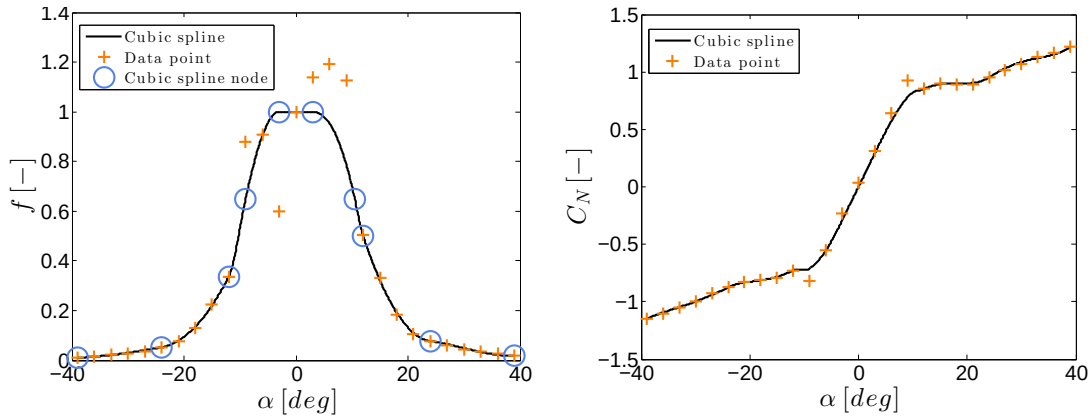

(a) function $f(\alpha)$ (b) function $C_N(\alpha)$

Figure 11: Cubic splines fitting of function $g(f)$ and corresponding $C_N(\alpha)$ for a flat plate

5.2.2 Computation of $g(f)$

In order to compute the aerodynamic moment, $g(f)$, generated by an airfoil as a function of the position of the separation point f, Beddoes used the following empirical relation

$$g(f) \equiv \frac{C_{m_{1/4}} - C_{m0}}{C_n} \tag{10}$$

where $C_{m_{1/4}}$ is the moment coefficient at the quarter chord and C_{m0} is the zero lift moment coefficient.

As with $f(\alpha)$, $g(f)$ can be curve fitted from experimental data. Once again, a series of cubic splines is used to carry out this curve-fit. However, $g(f)$ is not a single-valued function so two curve fits are performed: one for positive and one for negative values of $\alpha^{'}$.

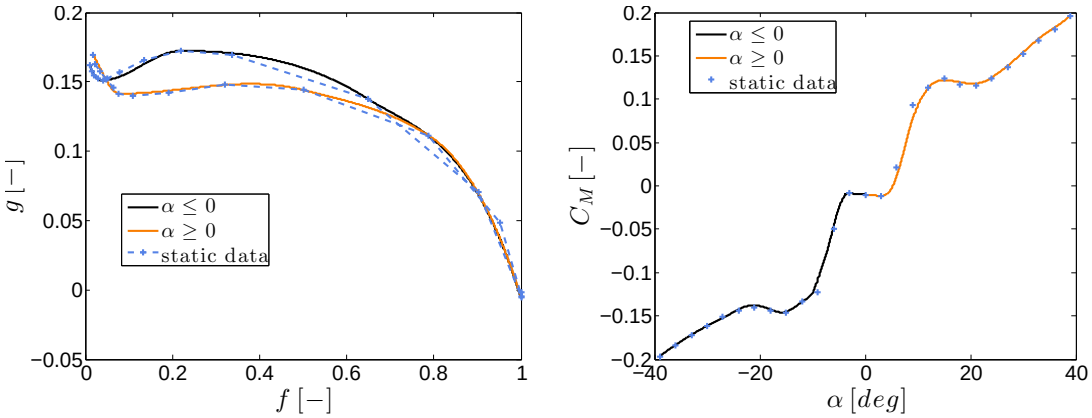

(a) function $g(f)$ (b) function $C_M(\alpha)$

Figure 12: Cubic spline fitting of function $g(f)$ and corresponding $C_N(\alpha)$ for a flat plate

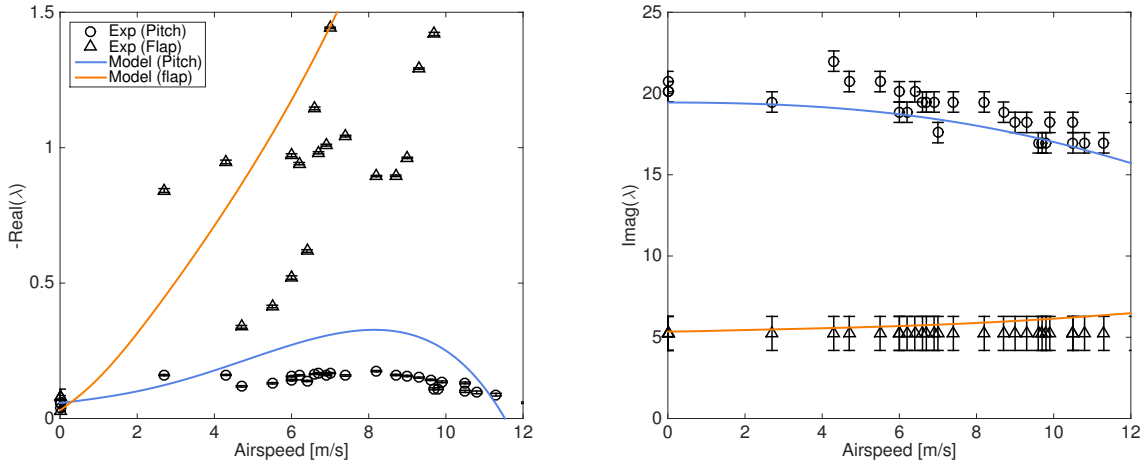

(a) Real part

(b) Imaginary part

Figure 13: Comparison of the variation of the modal parameters of the pitch and the flap obtained from experiments and from the linear aerodynamics model

6 COMPARISON OF THE EXPERIMENTAL RESULTS AND THE MODELS

This section aims to compare three aeroelastic models of the NLPFW. The structural equations are the same in all three models, the difference lying in the aerodynamic modelling:

- Linear aerodynamics
- Full LB model
- LB model with the leading edge vortex module turned off.

6.1 Subcritical airspeeds

The variation of the system's effective damping and frequency with airspeed obtained from the experiments and from the linear aerodynamic model is plotted in Fig. 13. The frequency is predicted well for both modes (Fig.13(a)) but the damping (Fig.13(b)) is over-estimated by the model; it is about twice as large as the measured damping for both the pitch and the flap. The method used to compute the damping from the experimental results (Hilbert transform + exponential fitting) is subject to four problems that might artificially reduce the damping estimate. Firstly, since there is a coupling between the pitch and the flap, the signal used to compute the flap damping does not decay to zero because it is excited by the pitch, which is lightly damped. Secondly, the setup is subject to wind turbulence which means that its response never really decays to zero. Thirdly, the flap is so highly damped that it undergoes only one or two oscillations before it decays. Fourthly, in order to measure several oscillation cycles, the initial angle from which the setup was released was higher than the stall angle, which means that the linear aerodynamics model is too simple.

6.2 Supercritical airspeeds

The comparison of the pitch LCO amplitude variation with airspeed obtained from the experiments and the models is depicted in Fig.14. All three models predict the low amplitude oscillations with a satisfying accuracy up to the jump, then they fail. The linear and LB without vortex models do not predict an amplitude jump at all. The full LB model predicts a huge jump in amplitude, much bigger than the one observed experimentally. It must be stressed that the parameter values of the full LB model were chosen in order to obtain an amplitude jump at the right airspeed. It is possible that these values can be better tuned in order to obtain the right amplitude values after the jump.

The flap amplitude is slightly over estimated by the linear model and behaves strangely after the jump for both version of the LB model, as seen in Fig.14(c). This strange behaviour is probably due to the large pitch amplitude and to the coupling between the pitch and the flap on the full LB model; it may vanish if the pitch amplitude is predicted with more accuracy.

The conclusions drawn on the pitch results also apply to the frequency predictions, as shown in Fig.14(b). Once again, all three models are reasonably accurate up to the jump and then fail for different reasons. The absolute accuracy of the pre-jump predictions is around 0.2 Hz, which is adequate.

Finally all models fail to represent the variation of the mean pitch and flap angles, as shown in Fig.14(d). The linear model predicts zero mean angular displacements at all airspeeds. The two LB models predict zero displacements up to the jump. It should be stated that the mean flap displacement measured experimentally may be due to inaccuracies in the setting of the pitch angle. In that case, the model predictions are actually accurate.

These early results show that the linear model is good enough for low amplitude LCO prediction and that a non-linear aerodynamic model can represent a jump similar to the one observed experimentally. Further work must be carried out in order to improve the post-jump predictions and to determine if the jump is caused by dynamic stall.

7 CONCLUSION

The NLPFW is a novel setup that features complex aerodynamic and structural nonlinear effects, leading to interesting bifurcation behaviour. Modelling this setup remains a challenge, although some encouraging results were obtained. Firstly, a simple nonlinear structural model coupled to linear aerodynamics successfully predicted the low amplitude bifurcation behaviour of the system with an absolute error smaller than 0.5m/s in airspeed, 0.2 Hz in LCO frequency and 0.005 rad in Amplitude. Secondly, an improved version of the Leishman-Beddoes model showed that the jump observed could be due to dynamic stall, however the model is not accurate enough to predict the post-jump behaviour. Future work will aim at improving the stall model by adapting the parameter values. Detailed static and dynamic measurements of the aerodynamic loads acting on the wing will be collected and used to select the new parameter values.

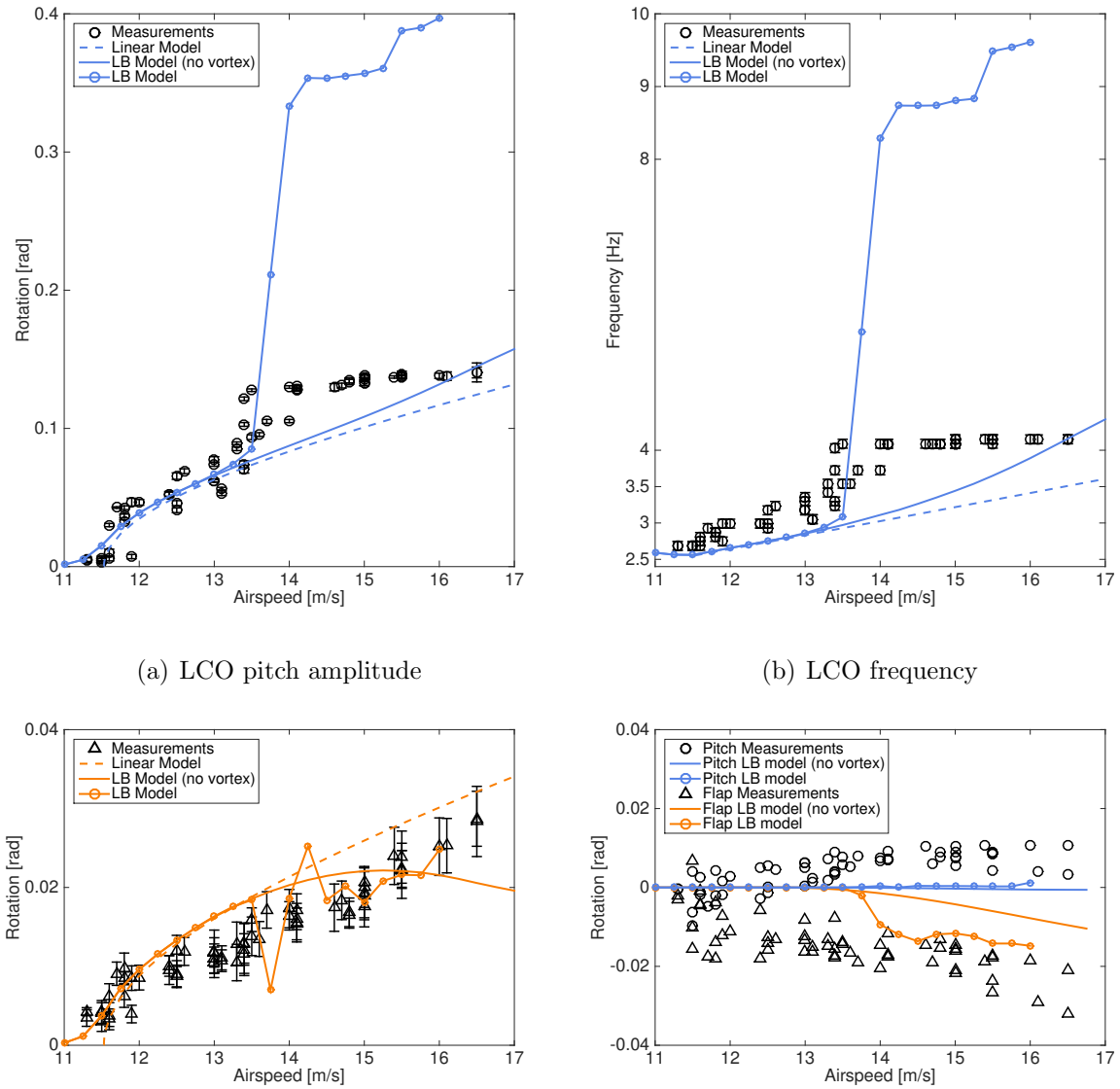

(a) LCO pitch amplitude

(b) LCO frequency

(c) LCO flap amplitude

(d) LCO Average amplitude

Figure 14: Comparison of the variation of the LCO frequency and amplitude with the airspeed obtained from experiments and from the linear aerodynamics model.

8 ACKNOWLEDGMENTS

The authors would like to acknowledge the financial support of the European Union (ERC Starting Grant NoVib 307265).

9 REFERENCES

[1] O'Neil, T., Gilliat, H., and Strganac, T. (1996). Investigations of aeroelastic response for a system with continuous structural nonlinearities. In *AIAA, ASME, ASCE, AHS, and ASC, 37th, Structures, Structural Dynamics and Materials Conference*. Salt Lake City, UT.

[2] Conner, M., Tang, D., Dowell, E., et al. (1997). Nonlinear behavior of a typical airfoild section with control surface freeplay: a numerical and experimental study. *Journal of Fluids and Structures*, 11(1), 89–109.

[3] Mukhopadhyay, V. (1999). Transonic flutter suppression control law design using classical and optimal techniques with wind-tunnel results. In *40th AIAA/ASME/ASCE/AHS/ASC Structures, Structural Dynamics and Materials (SDM) Conference*. St. Louis, MO: AIAA.

[4] Abdelkefi, A., Vasconcellos, R., Nayfeh, A., et al. (2012). An analytical and experimental investigation into limit-cycle oscillations of an aeroelastic system. *Nonlinear Dynamics*, 71(1-2), 159–173.

[5] Tang, D. and Dowell, E. (2011). Aeroelastic response induced by free play, part 2: Theoretical/experimental correlation analysis. *AIAA Journal*, 49(11), 2543–2554.

[6] Dimitriadis, G. and Li, J. (2009). Bifurcation behavior of airfoil undergoing stall flutter oscillations in low-speed wind tunnel. *AIAA Journal*, 47(11), 2577–2596.

[7] Poirel, D. and Mendes, F. (2012). Experimental investigation of small amplitude self- sustained pitch-heave oscillations of a naca0012 airfoil at transitional reynolds numbers. In *50th AIAA Aerospace Sciences Meeting including the New Horizons Forum and Aerospace Exposition*. Nashville, Tennessee.

[8] Razak, N. A., Andrianne, T., and Dimitriadis, G. (2011). Flutter and stall flutter of a rectangular wing in a wind tunnel. *AIAA Journal*, 49(10), 2258–2271.

[9] Amandolese, X., Michelin, S., and Choquel, M. (2013). Low speed flutter and limit cycle oscillations of a two-degree-of-freedom flat plate in a wind tunnel. *Journal of Fluids and Structures*, 43, 244–255.

[10] Platten, M., Wright, J., Cooper, J., et al. (2009). Identification of a nonlinear wing structure using an extended modal model. *Journal of Aircraft*, 46(5), 1614–1626.

[11] Hancock, G., Wright, J., and Simpson, A. (1985). On the teaching of the principles of wing flexure-torsion flutter. *Aeronautical Journal*, 89, 285–305.

[12] J.G. Leishman, T. S. B. (1989). A semi-empirical model for dynamic stall. *Journal of american helicopter society*, 34, 3–17.

[13] W. Sheng, F. N. C., R. A. McD. Galbraith (2008). A modified dynamic stall model for low mach numbers. *Journal of Solar Energy Engineering*, 130, 31013.

[14] Bisplinghoff, R., Ashley, H., and Halfman, R. (1996). Aeroelasticity. Dover Publications Inc.

[15] Fung, Y. (1993). An introduction to the Theory of Aeroelasticity. Dover Publications Inc.

[16] Lee, B., Gong, L., and Wong, Y. (1997). Analysis and computation of nonlinear dynamic response of a two-degree-of-freedom system and its application in aeroelasticity. *Journal of Fluids and Structures*, 11, 225–246.

[17] Leishman, J. G. (2006). Principle of Helicopter Aerodynamics. Cambridge University Press.

10 COPYRIGHT STATEMENT